COBEM 2023 27TH INTERNATIONAL CONGRESS OF MECHANICAL ENGINEERING

ABCM Brazilian Society of Mechanical Sciences and Engineering
27th ABCM International Congress of Mechanical Engineering
December 04-08, 2023, Florianópolis-SC, Brazil

COB-2023-0684
LASER DIRECTED ENERGY DEPOSITION PROCESS OPTIMIZATION PARAMETERS FOR AISI 410L SINGLE LAYERS

Jurandir Marcos Sá de Sousa
Precision Engineering Laboratory, Federal University of Santa Catarina, Campus Reitor João David Ferreira Lima, s/n°, Trindade, Florianópolis, SC - 88040900, Brazil.
Senai Innovation Institute for Manufacturing Systems and Laser, Arno Waldemar Döhler, 308, Santo Antônio, Joinville, SC - 89218153, Brazil.
jurandirmarcos37@gmail.com

Milton Pereira
Precision Engineering Laboratory, Federal University of Santa Catarina, Campus Reitor João David Ferreira Lima, s/n°, Trindade, Florianópolis, SC - 88040900, Brazil.
eng.milton@gmail.com

Henrique Santos Ferreira
Anselmo Thiesen Júnior
Juliane Ribeiro da Cruz
Senai Innovation Institute for Manufacturing Systems and Laser, Arno Waldemar Döhler, 308, Santo Antônio, Joinville, SC - 89218153, Brazil.
henrique.santos@sc.senai.br
anselmo.thiesen@sc.senai.br
juliane.alves@sc.senai.br

Abstract. *This work proposes a systematic method to find optimized laser directed energy deposition (L-DED) parameters based on single beads and single layers design of experiments (DoE) for AISI 410L stainless steel. As a differential, the method uses regression of data to map single layer features, and desirability factors to find an optimized parameter set based on the selected acceptance criteria. In the single beads stage, full factorial DoE is performed to reach stable process windows considering powder feed rate, laser power, and travel speed. Dilution, wettability angle, and efficiency were evaluated. The average width of single beads within the stable process window is used as a reference for the hatch spacing estimations. Then single layers were deposited with different processing parameters and the average height, dilution, waviness, layer slope, and efficiency were measured. An algorithm using regression analysis and desirability functions was employed to model these data and find L-DED parameters that best fit the user's acceptance criteria. A verification single layer was deposited using the L-DED parameters found by the algorithm to assess the model's prediction efficacy. Results showed that single layer's features found in both theoretical prediction and experimental verification exhibited very similar responses.*

Keywords: Laser cladding, prediction algorithm, stable set of parameters, refined microstructure, mechanical properties.

1. INTRODUCTION

AISI 410L stainless steel is applied in several parts, such as high-pressure pipes, pumps, bearings, cutlery, among others. In the martensitic state, this alloy is expected to show high mechanical strength and resistance to wear, besides superior corrosion performance at room temperature (Batista *et al.*, 2019). Laser directed energy deposition (L-DED) technology (ASTM F3187, 2016) has the potential to manufacture and/or repair parts on demand, eliminating the need for spare stocks, shortening lead time during maintenances, and preparing outdated items. Laser light's unique features aid in process dilution control, narrow heat-affected zones (HAZ), strength metallurgical bonds, and refined microstructures, all of which lead to high mechanical, tribological, and corrosive properties (Siddiqui and Dubey, 2021).

In this context, taking into account the intrinsic AISI 410L properties and L-DED technology benefits, processing AISI 410L parts using the L-DED turns up as an interesting alternative. In the literature, different authors, who investigated 410L stainless steel processed via L-DED, reported that, in general, the hardness, mechanical resistance, and tribological properties are based on microstructure fully martensitic, with refined grains, and strengthening phases precipitation (e.g. carbides) (Lai *et al.*, 2019; Huang *et al.*, 2019; Zhu *et al.*, 2021).

Despite the advantages provided, L-DED process complex thermal history (e.g. non-thermodynamic equilibrium, elevate G/R ratios, multiple and fast heating-cooling cycles) and the martensite nature (e.g. brittleness, uneven microstructure, deleterious phases precipitation) offer processing challenges and may impair the part or coating properties (Gradl *et al.*, 2022). To overcome these drawbacks, different approaches can be adopted. Performing design of

experiments (DoE) is an alternative and, for L-DED process, it generally comprises steps of single beads (SB, in which it is possible to vary all L-DED parameters to identify adequate SB section), and single layers (SL, in which suitable hatch spacing are investigated to avoid problems related to lack or excess overlap between SBs).

The SB cross-section analysis allow for the evaluation of geometrical parameters such as dilution, wettability angle and efficiency, that greatly impact metallurgical bond with the substrate (Mazaheri Tehrani *et al.*, 2020), the flatness level between the substrate and SB surface, that must be sufficiently high to avoid porosity and lack of fusion (De Oliveira *et al.*, 2005; Aghili and Shamanian, 2019) and the economic process viability, as operating inefficiently may not be a viable alternative (Reddy *et al.*, 2018; Gradl *et al.*, 2022). Besides, surface analysis of SBs also allow inspecting for the defects absence (e.g. cracks, porosities, delaminations).

For SL, in turn, hatch spacing (HS) is added as a variable. Dilution (D) and other relevant geometrical features can be measured such as average height (h), waviness ($\Delta h'$), slope (Θ), and efficiency (η). SL waviness and slope should be as low as possible since they can generate problems in 3D multilayer manufacturing (e.g. lack of fusion, standoff distance fluctuations, and distortions). As a best practice, the properties of h, $\Delta h'$, and Θ should only be measured in SL steady regions, because the initial SBs deposited may be in running-in regimes (e.g. powder flow stabilization, substrate temperature equalization) (Zhu *et al.*, 2011; Bax *et al.*, 2018; Reddy *et al.*, 2018).

SB and SL integrity is also impacted by L-DED hardware features [e.g. stand-off distance (Zhu *et al.*, 2011)]; powder nozzle design [e.g. coaxial or lateral (Nenadl *et al.*, 2014)]; laser source characteristics, build atmosphere condition [e.g. carrier and shielding gas flow, oxygen-content control (Song *et al.*, 2016)]; substrate [e.g. chemical composition, metallurgical compatibility (Lia *et al.*, 2017)], feedstock [e.g. powder particle size, morphology, rheology (Bax *et al.*, 2018)] exercise, and post-processes [(e.g. heat-treatments for stress relief, microstructure homogenization (Gradl *et al.*, 2022); laser remelting for defects mitigation and surface properties improvement (Paes *et al.*, 2022)].

Despite the fact that several works with studies of operational maps have been published in the literature, there is a lack of clear methods for obtaining the main L-DED parameters, particularly for single layer setups, as most of the studies found in literature consist of single bead DoE that, although fundamental, does not evaluate the interactions that occur due to lateral overlapping. A reliable SL DoE essential for the development of coating, parameters of repairs, and especially as a preliminary step for additive manufacturing by L-DED (AM L-DED), in which geometrical offsets unaccounted for can add up along multiple layers and lead to compromising defects.

In this context, the present work describes a method to find the main L-DED parameters (F, P, S, and HS) necessary for the deposition of defect-free SLs with well-established geometric selected acceptance criteria, so that they may even be interchangeable for other L-DED systems and materials.

2. EXPERIMENTAL PROCEDURES

This work is split into four main L-DED experimental sections, as illustrated by the Figure 1 flowchart:

1) Exploratory Stage: from single beads (SB), operational process windows and a stable set of L-DED parameters (powder feedrate F, g/min; laser power P, W; and travel speed S, mm/min) were established.
2) Modeling Stage: based on the evaluation of critical geometric properties of single layers (SL) deposited with varying hatch spacing (HS, mm) parameter, best hatch spacing fit is experimentally tested. Data obtained in this step is used as input for regression functions.
3) Optimization Stage: responses of the regressions were evaluated through the desirability function. generating as output a set of L-DED parameters (F, P, S, and HS) that, in theory, allow to simultaneously reach all the selected acceptance criteria regarding SL geometric properties. Experimental verification is performed aiming to attest to the set of L-DED parameters' consistency, and process repeatability.
4) Single Layer Characterization Stage: a SL cross-section sample deposited with the optimized L-DED parameters set is characterized about defects' absence, microstructure, and hardness.

2.1 Stage 1: Exploratory

This stage aims to find laser power (P), travel speed (S), and powder feedrate (F) L-DED parameters that result in continuous single beads (SB) within the selected acceptance criteria. At first, only the spot size was fixed in Ø1.78 mm. Operational process windows were investigated by searching the hardware thresholds. 2 F levels were selected, and "n" levels of P and S were varied until reaching a condition where continuous SBs were no longer formed. SBs were deposited at 25 mm in length on the substrate. Only the SB surfaces were qualitatively evaluated by optical stereoscope (OS) images.

SBs from the operational process windows were cut in cross-section, metallographically prepared, and analyzed by OS. SB cross-sections had their properties of dilution, D (Equation 1); wettability angle Θ, (Equation 2); and efficiency, η (Equation 3) data measured by ImageJ® software. To define the acceptance criteria, the frequency of occurrences statistical tool was applied, where quartile 1 (Q1) and quartile 3 (Q3) were taken as the lower and upper limits, respectively. From these, experimental data obtained were evaluated through regression functions and contour levels, until finding a stable set of parameters allowed meeting the acceptance criteria simultaneously (Figure 2).

$$D = B/(A + B) * 100\ [\%] \quad (1)$$

$$\theta = 180 - \arctan(2 * h/w)\ [\%] \quad (2)$$

$$\eta = (A * S * \rho)/F * 100\ [\%] \quad (3)$$

where A = deposited area (mm^2), B = molten area (mm^2), h = height (mm), w = width (mm), S = travel speed (mm/min), ρ = powder density (g/cm^3), and F = powder feedrate (g/min).

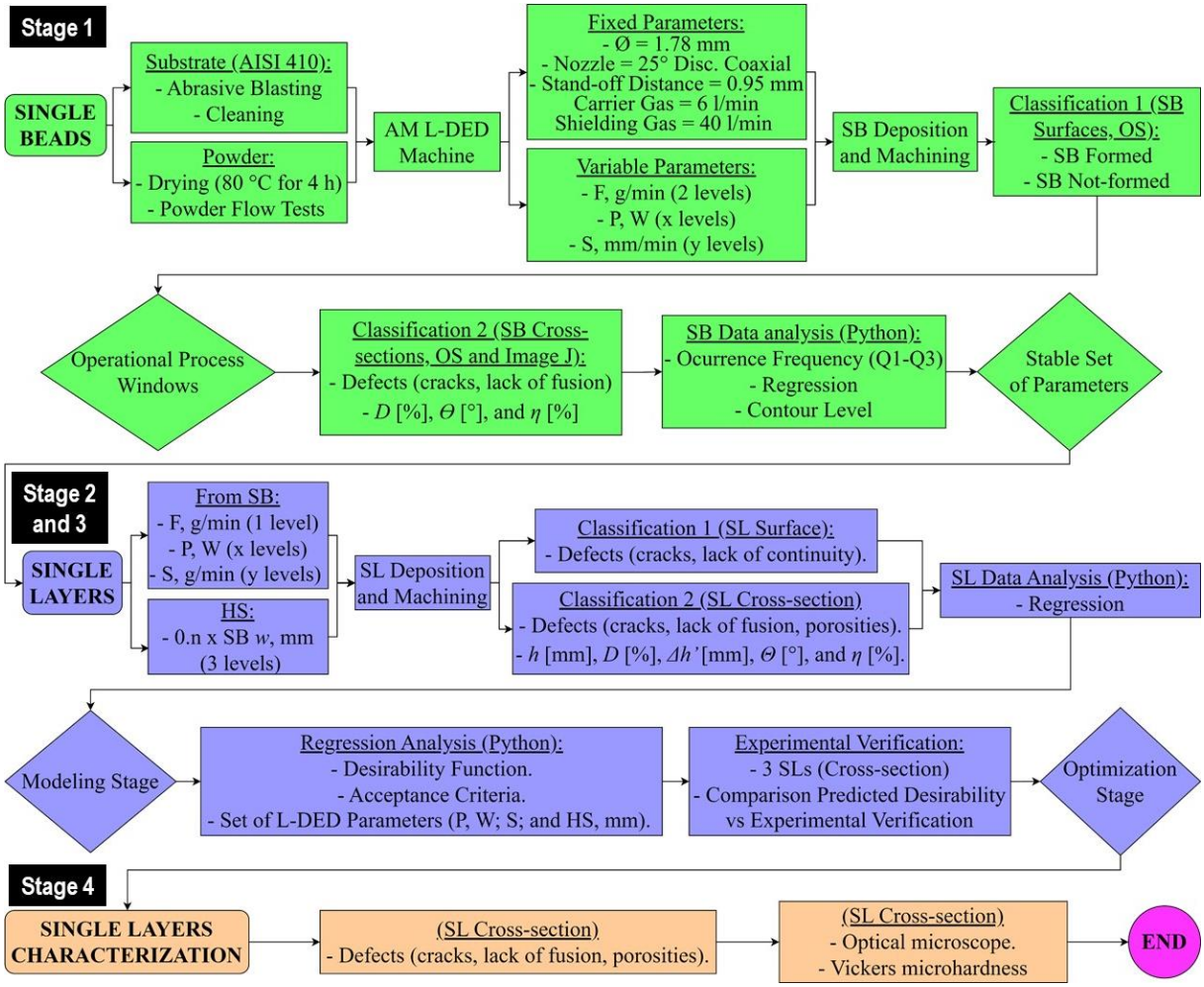

Figure 1. Experimental procedures flowchart.

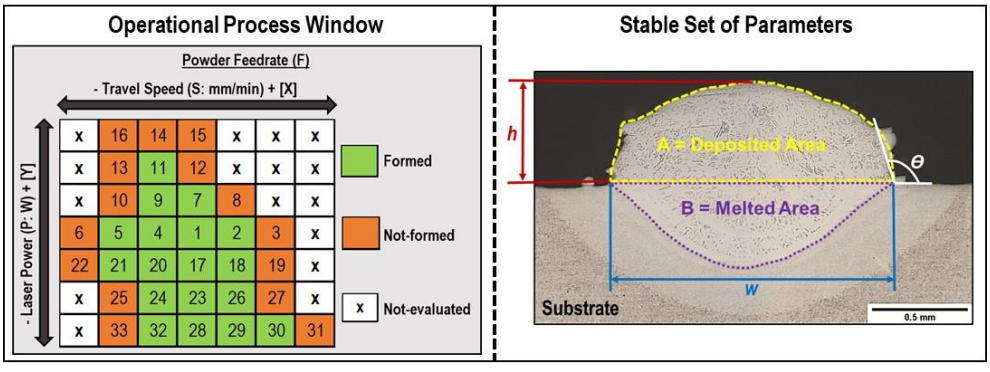

Figure 2. Illustrative scheme of the method used to find L-DED parameters in the SB stage.

2.2 Stage 2: Modeling

From the optimized parameter windows (P, S, and F) of Stage 1, a new full-factorial DoE is carried out, now also using hatch spacing (HS) as a variable, which aims to find an ideal lateral overlap between SB for obtaining defect-free single layers (SL) that meet acceptance criteria. The HS was selected as a percentage of the average width (w, 20, 30, and 50%) of the SBs from the optimized parameter windows (e.g. HS = 0.2*w). SLs were programmed with 10 SBs (25 mm

in length). After deposited, the resulting SLs were then cut in cross-section, metallographically prepared, and subjected to OS image capture. From these, a qualitative evaluation was performed to attest to the defects' absence (e.g. cracks, and lack of fusion). The approved SLs were then quantitatively analyzed about:

- Average height ($\bar{h}$): average distance between substrate surface and the last 3 SL peaks (P_1-P_3, Equation 4).
- Dilution (D): relation between melted area (B) and the sum of deposited area (A) and melted area (B) (Equation 1).
- Waviness ($\Delta h'$): relation between $\bar{h}$ and the last 3 SL valleys (V_1-V_3, Equation 5) was taken as waviness ($\Delta h'$, Equation 6).
- Slope (Θ): estimated through a straight row tangent to the SL surface. The 3rd (P_3) and last peaks (P_{10}) are set as references. As the peak is in the middle of SB, half the w is neglected in each of the reference SB (Equation 7).
- Efficiency (η): estimated through the relation between A and the number of SB, whose result is multiplied by the product between S and ρ. Finally, the entire relation result is divided by F (Equation 8).

$$\overline{h_P} = (P_1 + P_2 + P_3)/3\ [mm] \quad (4)$$
$$\bar{V} = (V_1 + V_2 + V_3)/3 \quad (5)$$
$$\Delta h' = \bar{h}/V\ [\%] \quad (6)$$
$$\Theta = tan^{-1}(P_3 - P_{10})/(0.7 * w)\ [°] \quad (7)$$
$$\eta = [((A/10) * S * \rho)/F] * 100\ [\%] \quad (8)$$

Figure 3 depicts an exemplary framework of the models used in the measurement of SL geometric properties. The experimental data resulting from these measurements are then analyzed mathematically in an empirical-statistical model through an algorithm based on a 3rd order polynomial multiple regression using the Minimum Square Errors method (developed in the Python® software), which was based on the literature (De Oliveira *et al.*, 2005).

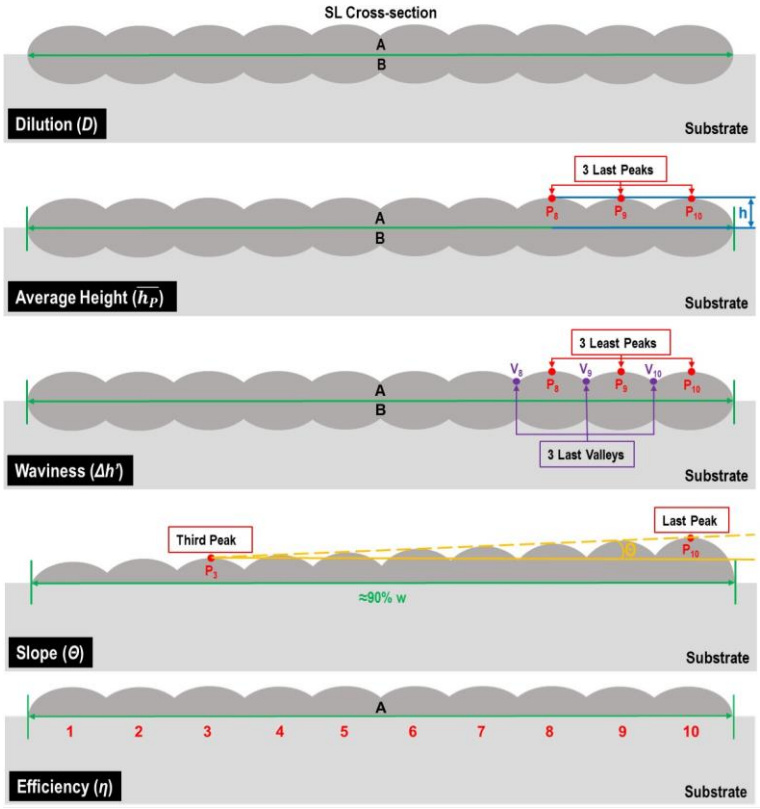

Figure 3. Illustrative scheme of the SL properties measurement.

2.3 Stage 3: Optimization

In this stage, responses of the regression functions from Stage 2 are simultaneously evaluated through the desirability function (Derringer and Suich, 1980) implemented in the algorithm. This function attaches a score to each of the regression responses so that the mean of all these individual scores gives the global desirability for a property aiming for one of the following objectives: maximization, minimization, or reaching a target. In this sense, from the response models of Stage 2, it is possible to determine the L-DED process parameters set (P, S, F, and HS) that provides the highest global desirability. The parameters set provided by the model are then verified experimentally through the deposition of SL in triplicate. The average results of the measured properties are compared to the model prediction (Figure 4).

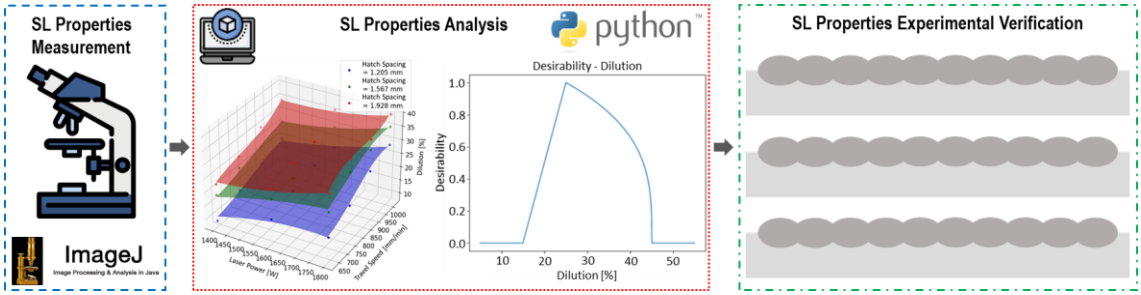

Figure 4. Illustrative scheme of the method and tools used in the optimization stage.

2.4 Stage 4: Single layer characterization

One of the SLs from the experimental verification step was metallographically prepared, and evaluated by Optical Microstructure (OM), and Vickers microhardness, aiming to verify the metallurgical bond integrity at the substrate/single layer interface, as well as the main characteristics of the microstructure and hardness in the different regions.

3. MATERIALS AND EQUIPMENTS

This section details the structure required for this work's experimental accomplishment.

3.1 Substrate and feedstock

For the SB and SL deposition, hot-rolled AISI 410 MSS plates (300 x 75 x 16.5 mm) were used as the substrate. Before deposition, substrates were blasted and cleaned in ethyl alcohol. Gas-atomized AISI 410L MSS 53-150 µm powder (Höganäs S/A) was employed as feedstock. Table 1 brings the chemical composition of the substrate and feedstock.

Table 1. Chemical composition of the 410 MSS substrate, and 410L MSS feedstock.

Elements (wt.%)	Cr	Mn	Si	Ni	C	S	Fe
410 MSS Substrate	13.5	1.0	1.0	0.7	0.15	0.03	Bal.
410L MSS Feedstock	12.2-13.5	0.6-1.0	0.6-1.0	0.1-0.9	0.02-0.03	0.01-0.03	Bal.

3.2 L-DED machine system

L-DED machine used was the RPMI 535® from RPM Innovations Inc. This is coupled to a continuous 100 µm fiber laser source doped with Ytterbium (Yb) with a maximum laser power of 3300 W (YLS-3000-CT) and 1064 nm ʎ from IPG Photonics®. The Beam Parameter Product (BPP = 10.0), and the Beam Quality Parameter (M^2 = 29.7) were measured using the Focus Monitor FM+ beam profilometer from PRIMES GmbH. A 25° discontinuous 4-coaxial nozzle was used.

3.3 Characterization

An optical stereoscope (OS, ZEISS V8) was used to certify the defects' absence on the surfaces of the SBs and SLs, as well as the capture of cross-sectional images for later measurement of geometric properties using the Image J® software. Samples cross-section machined, metallographically prepared by sanding (#80-1200 Mesh), polishing (0.3 um diamond solution suspension), and chemical etching (Ralph's reagent). In the optimized SL characterization, optical microscopy (OM) ZEISS AXIO M2M, was used. Hardness was measured using a Vickers WILSON 402 MVD tester.

4. RESULTS AND DISCUSSION

This section describes the main results. Further information can be found in Thiesen Jr.'s (2021) master thesis and the Authors also utilized some of its principles in a paper published and presented at COBEM 2021 (Sousa *et al.*, 2021).

4.1 Stage 1: Exploratory outcomes

As the Stage 1 method describes (item 2.1), operational maps were plotted (Figure 5), which illustrate the laser power (P) and travel speed (S) ranges, which consolidated single beads (SB) for each powder feedrate (F) evaluated. Regarding P, its elevation extended the maps to larger S values, in all F windows (e.g. S=1600-S=1800 mm/min). This factor then governed the lower P limits, which may be related to insufficient energy density (J/mm) to melt the powder and a portion of the substrate. Concerning S, with F increase, there was a displacement of the operational region for higher P ranges, owing to the fluctuation in the powder amount per unit length (g/mm) and the sufficient energy density. Regarding F,

expansion in the operational map is according to its elevation. This behavior can be linked to the fluctuation in the powder amount per unit length, and the energy density required to melt it (Bax *et al.*, 2016; Mazaheri Tehrani *et al.*, 2020).

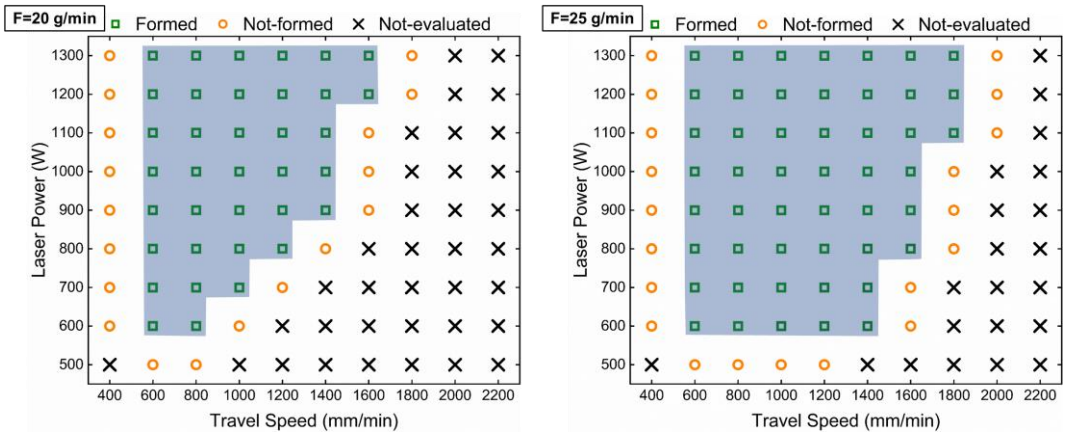

Figure 5. L-DED parameter windows for the operation maps achievement.

In the stable set of parameters, SB cross-sections from operational process window were prepared metallographically and analyzed. Minimum and maximum thresholds (Q1 and Q3) did not show prohibitive values, to the point of generating lack and/or excess of fusion as for *D* (35-45%) (Mazaheri Tehrani *et al.*, 2020), defects between single beads concerning Θ (110-132°) (Siddiqui and Dubey, 2021). Figure 6 shows the regressions between L-DED parameters (input) and SB properties (output). The *D* was governed by P (36% increase between 700 W and 1300 W) and F (24% increase between 20 g/min and 25 g/min). Higher P and S ranges, allied to lower F, resulted in higher values. On the other hand, lower *D* was watched in the lower P and S ranges. P increase enhances heat input on the substrate. Higher S promotes a lower powder amount per unit length and decreases the heat input on the substrate. F increment provides a higher absorption of the heat required to melt the greatest amount of powder added, which reduces heat input into the substrate (Aghili and Shamanian, 2019). The Θ was proportional to S (36% increase between 600 and 1800 mm/min). Concerning F, a 10% reduction was noted between 25 g/min and 20 g/min. This result is explained by the decrease in powder amount per unit length and elevation in energy input per unit length, which rise the molten pool heating and widens the SB (De Oliveira *et al.*, 2005). The η was proportional to P, followed by S and F. In the P axis, it was verified that η increased two times with elevation from 700 W (η≈14%) to 1300 W (η≈28%). S also exerts a significant influence (21% decrease between 600 and 1600 mm/min). With P increasing and F decreasing, the catchment and melting of the powder particles in the molten pool increased. With S reduction, laser beam/feedstock-substrate interaction time increased, elevating the energy available to melt the powder, and η (Reddy *et al.*, 2018). For all selected acceptance criteria to be met simultaneously, it is necessary to know the intersection between the response surfaces and reference planes of acceptance criteria (Figure 6). A wider stable set of parameters (highlighted in gray) was delivered by F=25 g/min, which was then selected for the next Stage (Single Layers, SL). P and S matrices, in turn, were assembled from the within ranges.

4.2 Stage 2 and 3: Modeling and optimization outcomes

Single layers (SL) are constituted by lateral SBs deposited and partially overlapped. From the stable set of parameters (F, P, S) defined in the exploratory Stage 1 (SB), SL Stage 2 investigates the hatch spacing (HS) parameter that results in defect-free SLs within the selected acceptance criteria. As stated in item 2.2, HS was determined by referencing the average width (*w*) of the approved SBs. Three levels (20, 35, and 50%) were tested. With the SLs properties measured, using the developed algorithm, the histograms of occurrence frequency were plotted. Table 2 shows the SL property findings for each HS value. After that, regression graphs were plotted (Figure 7). Observing curves of $\bar{h}$, there is an increasing trend inversely proportional to S and HS. *D* increased according to S and HS. The $\Delta h'$ was governed by HS. The Θ showed uneven behavior. Lower HS generated higher Θ, and S influence varied according to HS. The η was dependent on P. Similar connections are described in the literature for *D*, $\bar{h}$, and η (Reddy *et al.*, 2018; Aghili and Shamanian, 2019). Regarding $\Delta h'$ and Θ, highlights were found only on variation in the optimal standoff distance (Z-step) in 3D multilayer (AM L-DED), which might result in defect propagation (Zhu *et al.*, 2011).

Table 2. Average values of SL properties and occurrence frequency histograms.

HS (mm) / SL Property	*D* (%)	$\bar{h}$ (mm)	$\Delta h'$ (%)	Θ (°)	η (%)
1.10	43	0.5	17.7	0.4	15.2
0.90	38	0.6	11.6	0.5	14.6
0.70	27	0.7	6.7	1.5	14.7
From Histograms	15-53	0.3-1.3	5-30	0.0-2.5	13-23

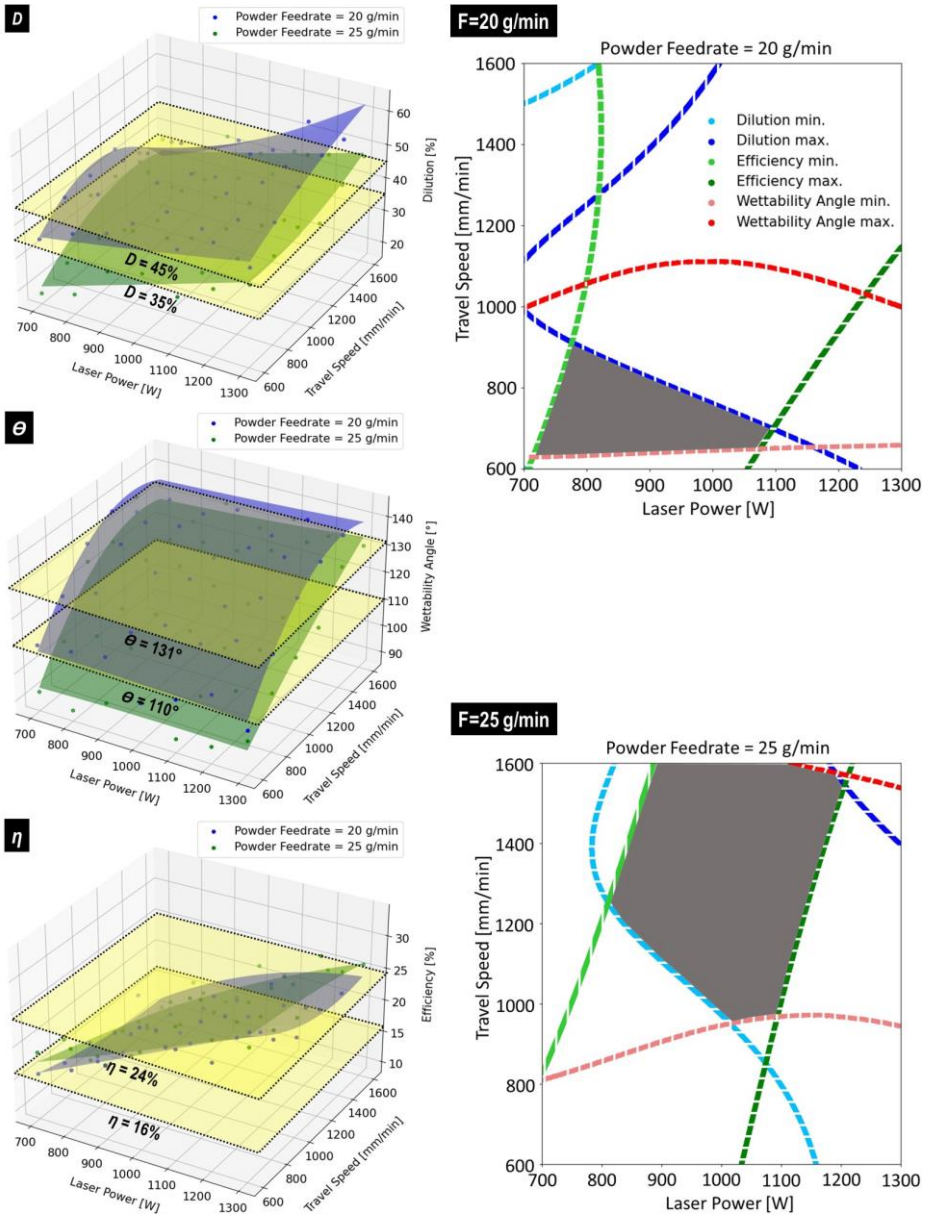

Figure 6. Regression functions and stable set of L-DED parameters for single beads deposition with properties within the selected acceptance criteria.

For Stage 3 (Optimization), regression responses were analyzed simultaneously in desirability function, where values (minimum, target, maximum) were stated (Table 3). The maximum D, $\Delta h'$, Θ, and minimum η were stipulated based on the literature (Zhu *et al.*, 2011; Reddy *et al.*, 2018; Mazaheri Tehrani *et al.*, 2020). For this reason, no values were estimated in target functions for these properties. Algorithm-predicted properties were added to the "predicted SL properties" row of Table 3. For experimental verification, employing the algorithm L-DED optimized parameters (Figure 8 board), three SL samples were deposited. After metallographic preparation, SL properties average values obtained were added to the “experimental SL properties” row of Table 3. Comparing the “predicted” vs “experimental” average rows, accentuated differences was noticed only for Θ, due to the multiple influence variables involved in terms of measuring.

Table 3. Acceptance criteria imposed on the desirability function and SL properties (algorithm predicted vs. experimental verification).

Desirability Function Type	D **(%)**	$\bar{h}$ **(mm)**	$\Delta h'$ **(%)**	Θ **(°)**	η **(%)**
Minimum	15	0.5	0.0	0.0	20.0
Target	25	0.7	-	-	-
Maximum	45	0.9	30.0	2.0	100
Algorithm Predicted SL Properties	35	0.84	11	0.42	19
Experimental Verification SL Properties	33	0.94	13	0.88	23

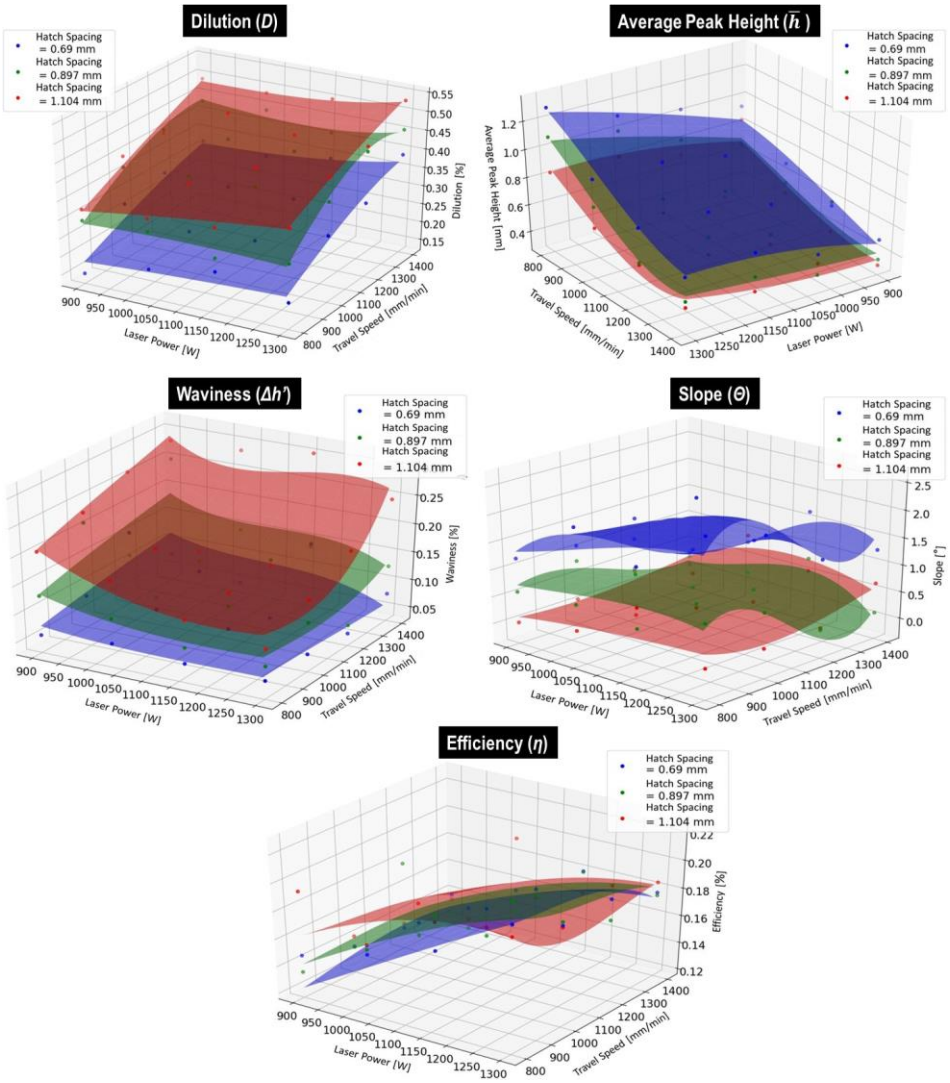

Figure 7. Regression functions of the SL properties evaluated.

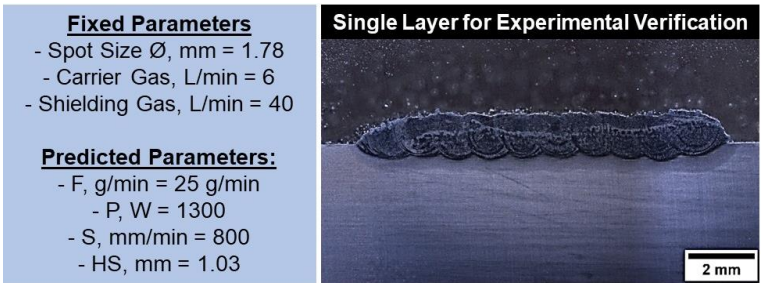

Figure 8. Algorithm predicted L-DED parameters, and SL cross-sections deposited for the experimental verification.

4.3 Characterization outcomes

Figure 9 shows the optical microstructure of the SL deposited with L-DED optimized parameters. It is worth noting that there were no lack of fusion, delamination, and cracks. The absence of these defects implies that the L-DED parameter selection method employed was effective. Microstructure exhibited refined constituents (dark regions) dispersed in a lighter-shade matrix. Based on literary descriptions, dark constituents observed are probably martensite, and their formation were triggered by the substrate's high C-content, laser's fast cooling rate, and improved heat sink through conduction mechanism near the substrate. Lighter regions should be ferrite and a portion of retained-γ. At the grain boundaries, constituents with a second-phase character are possibly carbides. It was noted that the boundaries between SBs were predominantly ferritic, and with very refined precipitates, which can be attributed to a tempering effect, due to the heating/cooling cycle imposed by the SB deposited later. The HAZ was narrow, and probably quenched, surrounding the SBs. Substrate martensite was probably tempered (Lai *et al.*, 2019; Zhu *et al.*, 2021).

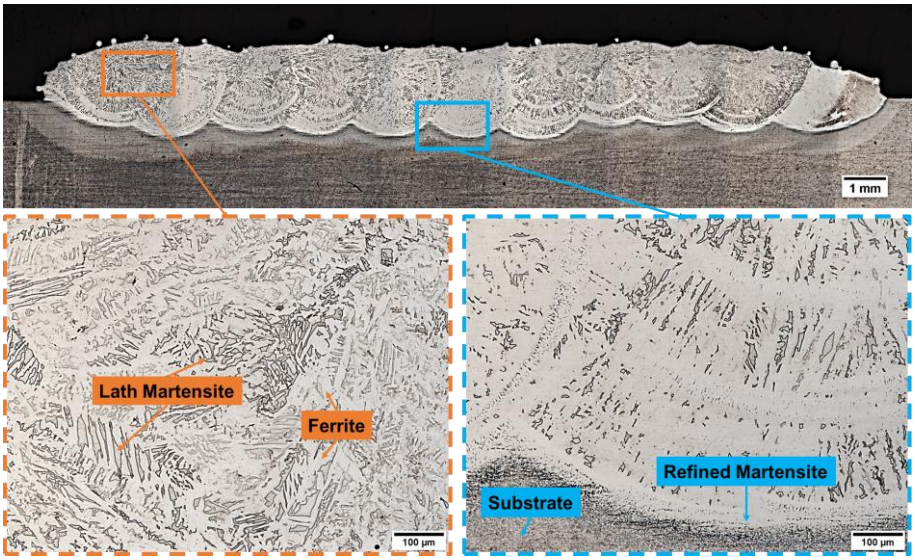

Figure 9. SL optical microstructure, highlighting specific regions' features.

Figure 10 graph show the SL microhardness profile. The average SL microhardness was 398 HV. It was verified a transition region with higher values and harsh fluctuation, comprising dilution and HAZ. The average value of these regions was >450 HV. For both parameters, just above 200 HV, steady was observed, attesting to the annealed substrate microstructure meeting. Microhardness peak observed in the transition region can be attributed to the more refined martensite and the higher C-content coming from the substrate. The higher C-content in this area is owing to the dilution effect with the substrate and the laser's fast cooling rate, which does not provide enough time for a significant amount of this C to migrate to the upper single layer region. Owing to dilution with C-rich substrate and the refined microstructure, values of 450-490 HV are recorded at the transition regions (Lai *et al.*, 2019; Huang *et al.*, 2019).

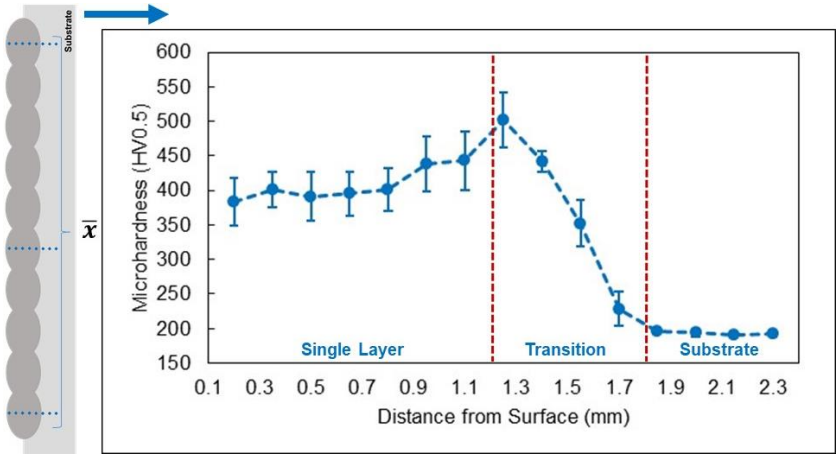

Figure 10. SL microhardness profile.

5. CONCLUSIONS

This paper offered L-DED parameterization research based on multiple well-defined Stages, aiming at optimizing the major parameters of this process in single bead and single layer setups:

- Exploratory Stage 1 enabled the establishment of operational maps, as well as stable processing ranges that assured single beads with geometric properties that matched the selected acceptance criteria.
- Stages 2 and 3 allowed for the observation of geometric property trends, verification of the parameters with the greatest influence on a specific property, and the identification of optimized L-DED parameters set that provided single layers free from defects and within the acceptance criteria.
- Microstructure analysis in Stage 4 confirmed the defects' absence as well as the strength metallurgical bond at the substrate/single layer interface. The observed characteristics agreed with literature, pointing to a biphasic ferrite/martensite microstructure with the potential of retained austenite and refined carbides at the grain boundaries.
- Microhardness profile represented the microstructure features, with an even average in the coarser ferrite microstructure single layer, followed by a peak in the transition area, which showed carbon-rich refined martensite.

6. AKNOWLEDGEMENTS

We thank to Precision Engineering Laboratory, Federal University of Santa Catarina, and Senai Innovation Institute for Manufacturing Systems and Laser Processing for their technical-scientific support.

7. REFERENCES

Aghili, S. E., Shamanian, M., 2019, Investigation of powder fed laser cladding of NiCr-chromium carbides single-tracks on titanium aluminide substrate, *Optics and Laser Technology*, Vol. 119, pp. 105652.

ASTM F3187, "Standard Guide for Directed Energy Deposition,", 2016, *ASTM International*. American Society for Testing and Materials, Pennsylvania, pp. 1–22.

Batista, M. N., Marinelli, M. C., Alvarez-Armas, I., 2019, Effect of initial microstructure on surface relief and fatigue crack initiation in AISI 410 ferritic-martensitic steel, *Fatigue and Fracture of Engineering Materials and Structures*, Vol. 42, pp. 61–68.

Bax, B., Rajput, R., Kellet, R., Reisacher, M., 2018, Systematic evaluation of process parameter maps for laser cladding and directed energy deposition, *Additive Manufacturing*, Vol. 21, pp. 487–494.

De Oliveira, U., Ocelík, V., De Hosson, J. T. M., 2005, Analysis of coaxial laser cladding processing conditions, *Surface and Coatings Technology*, Vol. 197, pp. 127-136.

Derringer, G., Suich, R., 1980, Simultaneous optimization of several response variables, *Journal of Quality Technology*, Vol. 12:4, pp. 214-219.

Gradl, P., Tinker, D. C., Park, A., Mireles, O. R., Garcia, M., Wilkerson, R., Mckinney, C., 2022, Robust Metal Additive Manufacturing Process Selection and Development for Aerospace Components, *Journal of Materials Engineering and Performance*, Vol. 31, pp. 6013–6044.

Huang, S., Li, D., Zhang, L., Zhang, X., Zhu, W., 2019, Tailoring the mechanical properties of laser cladding-deposited ferrous alloys with a mixture of 410L alloy and Fe–Cr–B–Si–Mo alloy powders, *Materials*, Vol. 12, pp. 1–12.

Khodabakhshi, F., Farshidianfar, M. H., Gerlich, A. P., Nosko, M., Trembo, V., Khajepour, A., 2019, Microstructure, strain-rate sensitivity, work hardening, and fracture behavior of laser additive manufactured austenitic and martensitic stainless steel structures, *Materials Science & Engineering A*, Vol. 756, pp. 545–5619.

Lai, Q., Abrahams, R., Yan, W., Qiu, C., Mutton, P., Paradowska, A., Soodi, M., Wu, X., 2019, Influences of depositing materials, processing parameters and heating conditions on material characteristics of laser-cladded hypereutectoid rails, *Journal of Materials Processing Technology*, Vol. 263, pp. 1–20.

Lia, F., Park, J., Tresler, J., Martukanitz, R., 2017, Partitioning of laser energy during directed energy deposition, *Additive Manufacturing*, Vol. 18, pp. 31–39.

Mazaheri Tehrani, H., Shoja-Razavi, R., Erfanmanesh, M., Hashemi, S. H., Barekat, M., 2020, Evaluation of the mechanical properties of WC-Ni coating on AISI 321 substrate, *Optics and Laser Technology*, Vol. 127, pp. 106138.

Nenadl, O., OCelík, V., Palavra, A., De Hosson, J. T. M., 2014, The prediction of coating geometry from main processing parameters in laser cladding, *Physics Procedia*, Vol. 56, pp. 220–227.

Paes, L. E.S; Pereira, M.; Xavier, F. A.; Weingaertner, W. L.; Vilarinho, L. O., 2022, Lack of fusion mitigation in directed energy deposition with laser (DED-L) additive manufacturing through laser remelting, *Journal of Manufacturing Processes*, Vol. 73, pp. 67–77.

Reddy, L., Preston, S. P., Shipway, P. H., Davis, C., Hussain, T., 2018, Process parameter optimisation of laser clad iron based alloy: Predictive models of deposition efficiency, porosity and dilution, *Surface and Coatings Technology*, Vol. 349, pp. 198–207.

Siddiqui, A. A., Dubey, A. K., 2021, Recent trends in laser cladding and surface alloying, *Optics and Laser Technology*, Vol. 134, pp. 106619.

Song, M., Lin, X., Liu, F., Yang, H., Huang, W., 2016, Effect of environmental oxygen content on the oxide inclusion in laser solid formed AISI 420 stainless steel, *Materials and Design*, Vol. 90, pp. 459–467.

Sousa, J.M.S.S., Gutjahr, J., Thiesen Junior, A., Ferreira, H.S., Pereira, M., and da Silva, L.J., 2021. "Laser directed energy deposition (L-DED) of AISI 410L: development of an operational map and the effect processing parameter on the bead geometry". In *Proceedings of the 26nd International Congress of Mechanical Engineering - COBEM 2021*. Florianópolis, Brazil.

Thiesen Jr., 2021. *Selection of processing parameters for the laser directed energy deposition process applied to additive manufacturing: a methodological proposal.* Master's thesis, Graduate Program in Engineering and Mechanical Sciences, Federal University of Santa Catarina, Joinville, Brazil.

Zhu, G., Li, D., Zhang, A., Pi, G., Tang, Y., 2011, The influence of laser and powder defocusing characteristics on the surface quality in laser direct metal deposition, *Optics and Laser Technology*, Vol. 44, pp. 349-356.

Zhu, H., Ouyang, M., Hu, J., Zhang, J., Qiu, C., 2021, Design and development of TiC-reinforced 410 martensitic stainless steel coatings fabricated by laser cladding, *Ceramics International*, Vol. 47, pp. 12505–12513.

8. RESPONSIBILITY NOTICE

The authors are the only responsible for the printed material included in this paper.